The Cryosphere, 20, 3683–3704, 2026
https://doi.org/10.5194/tc-20-3683-2026

The Cryosphere Open Access EGU

Wintertime evolution of landfast ice stability in Alaska from InSAR

Andrew Einhorn[1,2,3] **and Andrew Mahoney**[1]

[1]Geophysical Institute, University of Alaska Fairbanks, Fairbanks, 99775, USA
[2]Institute for Marine and Antarctic Studies, University of Tasmania, Hobart, 7001, Australia
[3]Australian Antarctic Program Partnership, Institute for Marine and Antarctic Studies, University of Tasmania, nipaluna/Hobart, Tasmania

Correspondence: Andrew Einhorn (andrew.einhorn@utas.edu.au)

Received: 12 February 2025 – Discussion started: 27 March 2025
Revised: 4 February 2026 – Accepted: 31 March 2026 – Published: 30 June 2026

Abstract. Landfast ice in Alaska is experiencing rapid changes in extent and duration, impacting the safety and utility of the ice for Arctic coastal communities. Current datasets of landfast ice only distinguish landfast ice from mobile pack ice, omitting crucial information regarding the relative safety of the ice. InSAR (Interferometric Synthetic Aperture Radar) holds promise for identification of landfast ice and measurement of centimeter-scale deformation from a spaceborne sensor. We use two InSAR-derived properties: coherence to identify areas of landfast ice, and the interferometric phase gradient to approximate a new metric called apparent strain (ϵ_a), which acts as a proxy for estimating the relative stability. Apparent strain is defined as the horizontal gradient of interferometric phase in the line-of-sight displacement. We built on a previous study Dammann et al. (2019), by assigning quantitative apparent strain values to identify three distinct stability classifications of landfast ice: Bottomfast ($\epsilon_a \leq 8.6\times10^{-6}$), Stabilized ($8.6\times10^{-6} < \epsilon_a \leq 2.4\times10^{-5}$), and Nonstabilized ($\epsilon_a > 2.4\times10^{-5}$). The monthly average apparent strain decreases as the season progresses, reaching the maximum stability in April or May depending on the region. This study introduces a novel approach to identify the relative stability for areas of landfast ice using InSAR. These findings have implications for enhancing the safety and planning of activities on landfast ice for Arctic coastal communities.

1 Introduction

1.1 Remote Sensing of Landfast Ice

Landfast ice, also commonly referred to as fast ice or shorefast ice, is sea ice that has become fastened to the coast and remains stationary for a period of time (Barry et al., 1979). Landfast sea ice is the most commonly encountered form of sea ice due to its proximity to Arctic coastal communities and its relative safety compared to drifting sea ice. Members of Arctic coastal communities use landfast ice for subsistence hunting and intercommunity travel, among other uses (e.g. George et al., 2004; Laidre et al., 2008). Landfast ice also serves as a habitat for marine mammals and shorebirds (Laidre et al., 2015; Lovvorn et al., 2014) and can be used for industrial purposes (Bieniek et al., 2022; Masterson, 2009). As a rigid barrier between the ocean and land, landfast ice can mitigate coastal erosion (Hošeková et al., 2021) and modify large-scale circulation patterns (Itkin et al., 2015; George et al., 2004; Laidre et al., 2008). The fundamental property of landfast ice that allows it to perform all these roles in the Earth system is its attachment to the land. Mahoney et al. (2006) proposed that this attachment could be determined from remote sensing data using two criteria: contiguity with the coast and immobility over time. Coastal contiguity can be determined from any single image with sufficient resolution to observe meaningful leads of open water, but determination of immobility requires at least two images of the same area acquired at different times. For example, Mahoney et al. (2007, 2014) analyzed triplets of co-located synthetic aperture radar (SAR) data spanning approximately

20 d to identify landfast ice in Alaska, while Fraser et al. (2012, 2020, 2021) and Cooley and Ryan (2024) derived landfast ice extent from 20 and 30 d composites of cloud-free moderate resolution imaging spectrometer (MODIS) data. Landfast ice is also identified in operational ice charts based on analysis of multiple images utilizing a range of satellite-based sensing methods (World Meteorological Organization, 2014). These various techniques of remote sensing produce similar information regarding the landfast ice in that the data is presented as a binary presence or absence of landfast ice within a grid cell. While these techniques are useful and valid for mapping landfast ice, the utility of landfast ice does not solely rely on the presence of fast ice but also the safety and stability, a measurement that these techniques and operational products cannot quantify. Interferometric Synthetic Aperture Radar (InSAR) has been shown to not only delineate landfast ice from mobile pack ice, but also measure centimeter- and millimeter-scale deformation within the fast ice (Dammann et al., 2016, 2018a, 2019; Dammert et al., 1998; Fedders et al., 2024; Li et al., 1996; Meyer et al., 2011; Morris et al., 1999), enabling the assessment of the landfast ice stability.

1.2 Interferometric Coherence

Interferometric coherence ($\hat{\gamma}$) is a measure of correlation between the two phase signals from a spaceborne radar and is generally only maintained over landfast ice, not pack ice. To perform an interferometric analysis between two SAR images acquired at different times, coherence must be maintained between the signal acquisition dates. Interferometry can be done when the two phase signals are of the same area acquired at different times (temporal baseline) and/or orbit positions (perpendicular baseline). Thresholding interferometric coherence to delineate landfast ice from mobile pack ice has been done before with the L-band ($\lambda = 23.6\,\text{cm}$) sensor Phased Array type L-band Synthetic Aperture Radar (PALSAR) aboard the Japanese satellite Advanced Land Observing Satellite (ALOS) (Meyer et al., 2011). The low frequency of PALSAR allowed for landfast ice to maintain coherence over long periods ($\sim 46\,\text{d}$). In addition to the long temporal baseline, the L-band wavelength of PALSAR allows the signal to be more resilient to decorrelating due to changes in the surface. Decorrelation (i.e. reductions of coherence) is likely the result of a combination of:

- errors in co-registration of the SAR images ($\gamma_{\text{processes}}$)
- changes in incidence angle (γ_{spatial})
- changes in the dielectric properties of the surface (γ_{thermal})
- deformation of the surface (γ_{temporal})

Examples of processes specific to sea ice which reduce coherence are redistribution of snow, melting and refreezing of the surface, ice deformation and motion, and rapid changes in salinity. Meyer et al. (2011) found that areas independently identified as mobile pack ice had an mean coherence ≤ 0.08, indicating total decorrelation while areas of landfast ice had a mean coherence of ~ 0.29 with an L-band SAR sensor. This analysis led Meyer et al. (2011) to define pixels that maintained normalized coherence values ≥ 0.1 over a 46 d period were classified as landfast ice. In addition, morphological filtering was needed to remove spurious non-contiguous pixels returning a coherence value ≥ 0.1. Meyer et al. (2011) did note that even with L-band, coherence was poor over thin landfast ice and after the onset of spring melt. Similarly when using the shorter wavelength C-band ($\lambda = 5.6\,\text{cm}$) SAR sensor aboard Sentinel-1, Dammann et al. (2019) observed generally poor coherence along the Alaska coastline in the Chukchi Sea due to suspected thin landfast ice and surface melting. Using Sentinel-1, Dammann et al. (2019) identified the boundary between zero and nonzero coherence to as the landfast ice edge. Both Meyer et al. (2011) and Dammann et al. (2019) selected SAR pairs from winter months (December–May) to maximize landfast ice extent and thickness while reducing the impacts of melt onset thus maximizing coherence. Coherence is required to perform interferometry between two SAR signals. Without coherence, phase, and thus deformation, cannot be measured accurately.

1.2.1 Interferometric Phase

The interferometric phase is one of the core measurements derived from interferometry as it can represent the amount of deformation that has occurred between signal acquisitions. The phase difference between SAR images is often called the interferometric phase, ϕ, primarily resulting from the effects of surface topography when viewed from two different positions, or line-of-sight surface displacement which occurred between image acquisitions when viewed from similar positions but different times. Over sea ice, where topographic expression is generally low, $< 10\,\text{m}$, variations in ϕ can be expected to be dominated by surface motion (Bamler and Hartl, 1998; Ferretti et al., 2007). Deformation in the across-track and vertical directions results in a phase change while InSAR is not sensitive to along-track deformation. The interferometric phase is commonly depicted by interferograms. Traditional interferograms consist of multicolored fringes where one fringe represents half a wavelength of deformation in the line-of-sight direction. The spatial rate at which the phase changes, phase gradient ($\nabla\phi$) provides insight and a measurement of the type and magnitudes of deformation occurring within the landfast ice. $\nabla\phi$ is calculated as:

$$\nabla\phi = \left(\frac{\partial\phi}{\partial x}, \frac{\partial\phi}{\partial y}\right) \tag{1}$$

indicating the change in phase in the across-track $\left(\frac{\partial\phi}{\partial x}\right)$ and vertical directions $\left(\frac{\partial\phi}{\partial y}\right)$. The interferometric phase

(Dammert et al., 1998), fringe patterns (Dammann et al., 2018b, 2019; Fedders et al., 2024; Morris et al., 1999; Pratt, 2022; Wang et al., 2020), phase difference (Li et al., 1996), and phase gradient (Dammann et al., 2019; Fedders et al., 2024) have all been used to approximate the deformation and stability of landfast ice. Inverse modeling of landfast sea ice deformation is possible from InSAR, but requires either in-situ observations of deformation and stressors or constraining the fringes to specific patterns (Dammann et al., 2016, 2018a; Fedders et al., 2024). Dammann et al. (2019) classified the deformation of landfast ice based on interferometric phase on a larger scale. They opted to directly interpret the phase information as representing the magnitude of strain rather than the inverse modeling approach which would also identify the type of strain. On large scales it is not feasible to use inverse modeling to determine the type and magnitude of strain. The key data to accurately constrain each area are not available. For studies in which the deformation cannot be restricted, directly interpreting the interferometric phase as a measure of the deformation is preferred.

The classification of landfast ice stability by Dammann et al. (2019) demonstrated the utility of interpreting fringes to represent the stability of landfast ice, but the definitions used were qualitative, thus difficult to reproduce and automate. Dammann et al. (2019) identified three stability zones based on the interferometric fringe pattern, orientation, and spacing:

- Bottomfast – No identifiable phase difference from the adjacent land
    - Same definition used by Pratt (2022)
- Stabilized – Poorly defined, widely spaced fringes, or abruptly reduced fringe spacing compared to offshore ice
- Nonstabilized – Well-defined fringe orientation or patterns

Dammann et al. (2019) associated the Stabilized zone with landfast ice that is sheltered by a point feature, while the Nonstabilized represents the floating extension, oceanward of any point features. While useful, these qualitative definitions can be subjective and are not easy to replicate between analysts. Hence we saw a need to quantitatively define these stability classes so that the process can automated. We build directly on the previous work of Dammann et al. (2018b, 2019); Meyer et al. (2011); Pratt (2022) to map the extent of landfast ice and develop a method for quantitatively definition of these stability zones using interferometric data from 12 d Sentinel-1 SAR pairings. To do so we defined a new metric called apparent strain (ϵ_a) which is derived from the interferometric phase gradient. Apparent strain describes the amount of line-of-sight deformation that InSAR is sensitive to, which occurred between satellite acquisitions. Having quantitative definitions of the stability zones defined by Dammann et al. (2019), using apparent strain, provides the opportunity to map the extent of these stability zones and to understand their evolution both intra- and inter-seasonally.

2 Data and Methods

2.1 Study Area

Our study area was chosen to coincide with that used in the development of the EM2025 landfast ice climatology (see Sect. 2.2) and includes waters of the US Arctic Outer Continental Shelf and adjacent waters in Canada and Russia. The coastlines extend from just west of Neshkan on the Chukotka Peninsula to the easternmost point of the Russian mainland in the Bering Strait and from the westernmost point on mainland Alaska, the Iñupiat village of Wales, to the Mackenzie Delta in Canada. To conform with prior analyses of landfast ice (Mahoney et al., 2007, 2014, 2024), our study area is divided into two regions (Fig. 1). The western region lies entirely within the Chukchi Sea and hereinafter is referred to as the Chukchi region, shaded cyan in Fig. 1. The eastern region includes a smaller area of the northern Alaskan Chukchi coast but is otherwise contained within the Beaufort Sea and hereinafter is referred to as the Beaufort region, blue shaded region in Fig. 1. The western and eastern regions meet at a point just west of Wainwright, Alaska.

2.2 EM2025 landfast ice climatology

The EM2025 landfast ice climatology (named after the same authors as this study and the year it was released) is a gridded daily dataset of landfast ice extent covering the study area depicted in Fig. 1 and spanning 1996–2023. A detailed description of the creation and results of the EM2025 dataset has been reported by Mahoney et al. (2024) and Mahoney and Einhorn (2026). In brief, the EM2025 dataset extends a previous SAR-based dataset of the same study area for the years 1996–2008 (Mahoney et al., 2014) using data derived from ice charts produced by the National Ice Center (NIC) and the National Weather Service's Alaska Sea Ice Program (ASIP). Here, we use landfast ice width data derived from the EM2025 dataset using the SLIEalyzer toolbox (https://github.com/armahoney/SLIEalyzer, last access: 14 June 2026), which computes the distance from the coast to the seaward landfast ice edge (SLIE) along a specified set of approximately coast-normal vectors, as illustrated in Fig. 1. Regions of the coastline which are not captured by the coast vectors are termed "shadow regions" and denoted with shaded yellow regions in Fig. 1 and all subsequent maps. Shadow regions occur due to complexities of the coastline such as small bays or straits. In these areas the coast-normal vectors intersect the coast mask multiple times. This approach provides a consistent spatial reference frame with which to measure the seasonal and interannual variations in landfast ice almost continuously at 8892 different locations

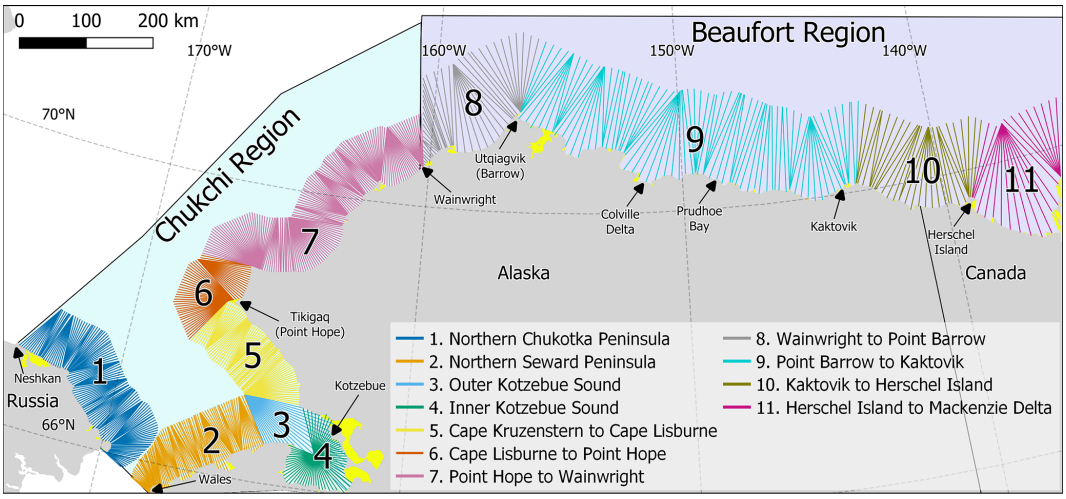

Figure 1. Spatial extent of the study area, two regions (Beaufort and Chukchi) and 11 sub regions. Every 10th coast-normal vector is displayed for each subregion in varying colors. Each vector is used to measure fast ice extent for both the InSAR method and EM2025 data. Yellow shaded regions represent "shadow regions" discussed in Sect. 2.2.

along the coast (6956 in the Chukchi region and 1936 in the Beaufort), spaced approximately every 200 m. It also allows us to calculate various statistics about the locations of the SLIE over different time periods.

2.3 InSAR-based detection of landfast ice

In this study, the term InSAR describes a signal processing technique for calculating the phase difference between two radar signals acquired from similar locations in space at separate times. Here, we use pairs of Sentinel-1 interferometric wide (IW) beam images with temporal and perpendicular baselines of 12 d and ≤ 300 m m respectively. These image pairs were selected using the Short Baseline Subset tool within the Alaska Satellite Facility (ASF) Vertex portal. Thirteen IW reference scenes were chosen exclusively on the basis of coverage of the study region. Six reference scenes were used to cover the Beaufort region while seven were used to cover the Chukchi region. In total, 2084 SAR pairs were identified between the months of November and July for the period from March 2017 to July 2022. These SAR scenes were multi-looked by 20×4 looks, resulting in pixel sizes of 80 m $\times$ 80 m. Multi-looking improves the signal-to-noise ratio and increases the interferometric coherence. We used ASF's Hybrid Pluggable Processing Pipeline (HyP3) toolbox (Hogenson et al., 2016) to produce interferometric data products in GeoTIFF format.

To obtain a useful ϕ value, the two SAR signals must remain sufficiently coherent between Sentinel-1's repeat orbits. The HyP3 toolbox (Hogenson et al., 2016) produces normalized coherence images where values of 0 indicate complete decorrelation and 1 indicates perfect coherence (Moreira et al., 2013). The magnitude of the reduction of coherence ($|\hat{\gamma}|$) can be estimated as:

$$|\hat{\gamma}| = \gamma_{\text{processes}} \cdot \gamma_{\text{spatial}} \cdot \gamma_{\text{thermal}} \cdot \gamma_{\text{temporal}} \quad (2)$$

By limiting our spatial baseline to ≤ 300 m and using constants specific to Sentinel-1 and C-band we can treat γ_{spatial} and γ_{thermal} as constants. In addition, we assumed that $\gamma_{\text{processes}}$ is 1, indicating there are no errors in the coregistration of the SAR pairs. These assumptions allowed us to attribute all variability in the reduction of coherence to deformation/displacement of the surface, γ_{temporal}.

In the context of sea ice, reductions of γ_{temporal} are assumed to be caused by ice drift or deformation, which is typically on the order of km d^{-1} for mobile pack ice. For drifting pack ice over a 12 d repeat orbit interval, γ_{temporal} is reduced to zero, resulting in decorrelation ($|\hat{\gamma}| = 0$). Fast ice by definition is stationary, but internal deformation still causes reductions of γ_{temporal}. However, for the landfast ice to remain landfast, the magnitude of this deformation needs to be relatively small so to not cause fracturing. The coherence will be reduced in highly dynamic landfast ice; landfast ice will have a higher coherence compared to adjacent pack ice. This principle has previously been used by Meyer et al. (2011) to delineate landfast ice from pack ice.

Meyer et al. (2011) demonstrated the ability to delineate landfast ice from mobile pack ice using a coherence threshold and morphological filtering in Alaska. The normalized coherence threshold used by Meyer et al. (2011) when using L-band PALSAR was 0.1. For this study, we use C-band which is more sensitive to smaller changes in the surface typically resulting in lower coherence values. The coherence threshold used by Meyer et al. (2011) cannot simply be assumed to be the same for the different wavelengths due to the increased sensitivity of C-band. For that reason we derived a C-band specific coherence threshold to delin-

eate landfast ice from mobile pack ice. A more detailed description of this derivation can be found in Section A1. In short, we used 14 SAR pairs, one from each month between December 2017–June 2018, from the Chukchi and Beaufort region. The Chukchi scene covered most of the northern Seward Peninsula and some of Kotzebue Sound. The Beaufort region scene covered the coastline west of Utqiagvik until approximately the Colville Delta. We applied thresholds ranging from 0.01 through 1.00 to the coherence images then applied morphological closing and opening operations to remove small and noncontiguous areas that exceed the threshold, which are likely noise. We then compared the areas identified by each threshold in each month to the extent of the minimum landfast ice extent identified in that month by the EM2025 dataset. The best threshold was then determined by the highest percentage of pixels that agreed with the corresponding EM2025 monthly minimum extent. The coherence threshold for delineating landfast ice from the mobile pack ice using C-band was determined to be 0.3 where areas which meet or exceeded this threshold were classified as landfast ice. This threshold was then applied to all normalized coherence images and used to measure landfast ice extent and to mask the interferograms, limiting our analysis to areas identified as landfast ice.

2.4 Calculation of apparent strain from phase gradient

After masking the interferograms with the coherence threshold, we used the magnitude of the interferometric phase gradient to derive the apparent strain in each interferogram. For short-baseline 12 d SAR pairs over sea ice, we can assume that variations in interferometric phase ϕ are dominated by variations in line-of-sight surface motion rather than by topography. ϕ is insensitive to motion perpendicular to the line of sight, but Fedders et al. (2024) has shown that it is possible to estimate two-dimensional horizontal strain of sea ice from the phase gradient, provided the phase slope is largely planar and the mode of deformation (e.g. radial divergence or rotation) is known. However, in general, derivation of two- or three-dimensional surface motion requires phase information from multiple look directions and the known deformation type. Instead, we define the term apparent strain (ϵ_a) to describe the magnitude of the horizontal gradient in line-of-sight displacement. Apparent strain can be calculated using the following:

$$\boldsymbol{\epsilon_a} = \frac{\boldsymbol{\lambda}}{4\pi(\Delta \boldsymbol{x})} |\nabla \phi| \tag{3}$$

Where λ is the C-band SAR wavelength (5.64 cm) of Sentinel-1 and $|\nabla\phi|$ is the magnitude of the phase gradient, given by:

$$|\nabla \phi| = \frac{\sqrt{\frac{\partial \phi}{\partial x}^2 + \frac{\partial \phi}{\partial y}^2}}{(\text{kernel length} - 1)} \tag{4}$$

Since ϕ is a cyclic quantity that wraps over an interval of 2π, we calculate $\nabla\phi$ following the approach described by Libert et al. (2022) whereby ϕ is first converted to a complex quantity, ϕ^*, with continuous real and imaginary components:

$$\phi^* = e^{i\phi} = \cos\phi + i\sin\phi \tag{5}$$

$$\frac{\partial \phi}{\partial x} = \angle\left(\frac{\partial \phi^*}{\partial x}\right) \tag{6}$$

$$\frac{\partial \phi}{\partial z} = \angle\left(\frac{\partial \phi^*}{\partial z}\right) \tag{7}$$

where $\angle$ indicates the argument of the complex exponent.

We approximate the partial derivatives in Eqs. (6) and (7) using finite differences across a 4 pixel window and insert them into Eq. (4) to derive the magnitude of the phase gradient. Apparent strain, ϵ_a, is then calculated using Eq. (3) and should be interpreted as the minimum net strain that occurred between SAR image acquisitions, since it only measures deformation along the satellite's line of sight. However, since it only represents displacement between two snapshots in time, it may underestimate the maximum strain that occurred during the 12 d period. As with the coherence images, we grouped ϵ_a results by month, according to the date of the primary image in each SAR pair, and mosaicked results to create images of monthly average ϵ_a for each of the Chukchi and Beaufort regions.

2.5 Spatial masks for defining apparent strain thresholds for stability

The Sentinel-1 SAR pairs used by Dammann et al. (2019) along the Alaskan Beaufort coastline do not follow the same strict temporal baseline requirement of 12 d between pairs, prohibiting the direct use of these SAR pairs during the derivation of apparent strain thresholds for each stability class, but will be used for later comparison. To account for this, we interpreted the landfast ice regimes associated with each stability zone and created masks that reflect the characteristics of landfast ice in each zone, but are usable in all years (Fig. 2). The spatial extents for each of these masks were determined independently of apparent strain values but instead by bathymetry, geomorphological characteristics, and features of the nearshore environment. These masks, which are shown in Fig. 2, represent areas that fit the characteristics of each landfast ice regime associated with each stability zone defined by Dammann et al. (2019). These stability zones were defined using the following criteria:

1. Bottomfast Landfast Ice (BFLFI) – Areas of the nearshore environment with a water depth shallower than 1.5 m (Danielson et al., 2015)

2. Sheltered Landfast Ice (SHLFI) – Areas between the seaward edge of the BFLFI edge and shoreward of any barrier islands. We acknowledge that barrier islands are not the only feature which anchor landfast ice.

3. not-sheltered Landfast Ice (NSHLFI) – Areas where landfast ice occurs seaward of any barrier islands. Note that this may include landfast ice stabilized by grounded ridges in addition to nonstabilized ice.

The bounds of the BFLFI mask were determined to be the area where water depth is between 0–1.5 m as these are the typical depths where bottomfast ice is found (Pratt, 2022). It is also important to acknowledge the difference between sheltered and stabilized terminologies in this instance. Sheltered landfast ice (SHLFI) is specifically landfast ice which is floating and anchored by barrier islands. The barrier islands shelter this landfast ice from dynamic interactions with waves and pack ice. SHLFI is likely to exhibit greater stability (lower apparent strain) compared to landfast ice anchored by grounded ridges, as barrier islands can better isolate landfast ice from ocean dynamics. The definition of the stabilized landfast ice zone by Dammann et al. (2019) includes landfast ice anchored by both barrier islands and grounded ridges. However, due to the location of grounded ridges not being consistent between seasons, we opted to use the areas sheltered only by barrier islands, SHLFI, as a representative area for the determination of an apparent strain threshold of the stabilized zone defined by Dammann et al. (2019). Given this definition and the spatial extent of SHLFI, we can assume that any landfast ice occurring within the SHLFI mask is anchored, thus representative of stabilized landfast ice, regardless of season. This also results in landfast ice that is grounded by ridges seaward of the barrier islands to be located within the NSHLFI mask, skewing the distribution of the NSHLFI toward a lower apparent strain. We then took the average of all apparent strain maps, on a per pixel basis, occurring in the Beaufort region during the month of April and derived the apparent strain thresholds for the three stability zones defined by Dammann et al. (2019) using a nonparametric optimization of the data within each mask independently.

3 Results

3.1 Landfast ice extent from coherence thresholds

Application of the coherence threshold described in Sect. 2.3 to 2084 SAR image pairs allowed us to produce a total of 30 monthly mosaics of landfast ice. These monthly mosaics represent the apparent strain for each month from December and May during the 2017–2021 landfast ice seasons. We used the SLIEalyzer toolbox (Sect. 2.2) to derive the average position of the SLIE over all seasons for each month for comparison with the equivalent results derived from the EM2025 dataset. For example, Fig. 3 compares positions of the InSAR-derived mean landfast ice extent during April (blue line) with that derived from the EM2025 dataset (cyan line) for the period 2017–2021. The SLIE positions show generally good agreement, with no consistent bias in the study region for this month. However, when averaging the difference between methods, the coherence mosaics tended to underestimate the landfast ice extent by between 1.5–5 km on average each month.

To compare the coherence-derived landfast ice extent against the EM2025 dataset for all months from December to May, we calculated the difference in monthly mean landfast ice width for each coast vector measured by the coherence-based method and the EM2025 dataset (Fig. 4). Differences were computed by subtracting the EM2025-derived widths from the coherence-derived widths; negative values therefore indicate underestimation by the InSAR-based approach. Figure 4 represents the difference in widths along the entire coastline where coast vectors from the Chukchi region are plotted in cyan while the Beaufort region is in blue. During December (Fig. 4A), mean landfast ice width was zero throughout much of the study region and both datasets generally agree where landfast ice had not yet formed. However, where landfast ice was present (primarily in the Beaufort region), the InSAR-derived results tended to underestimate the width. On average in the Beaufort region during December, the coherence method measured 5.1 km less landfast ice at each coast vector. This underestimation is reflected in the predominance of negative differences, with the blue line lying below the zero-difference line in Fig. 4A.

There is a similar pattern for the month of January (Fig. 4B), with the InSAR-based approach still tending to underestimate the width of landfast ice as it expands throughout both study regions. The tendency to underestimate persists until mid-winter, February, March, and April, during which the relationship becomes more variable along the coast, with the InSAR-based approach indicating more than 10 km more landfast ice than the EM2025 dataset at certain coast vectors (Fig. 4C–E). Although the average differences remain negative during the mid-winter months, with values of -5.1, -4.6, and -3.4 km from February to April in the Beaufort region, and -2.5, -3.7, and -1.5 km from February to April in the Chukchi region, these differences constitute only small percentages of the total landfast ice during this period. There is also notable spatial variability within the subregion, Inner Kotzebue Sound, during these months, with the difference in landfast ice width changing from < -10 km to > 10 km and back again over the span of just a few coast vectors. The cause of this variability is not certain, but examination of the primary SAR imagery and interferograms over Kotzebue Sound indicate that the surface of the ice loses coherence temporarily without any substantial horizontal motion. This coherence loss could be caused by surface flooding, which has been observed to be caused by heavy snow load in this region (Mahoney et al., 2021). Kotzebue Sound also has extensive areas of shallow water ($\sim \leq 2$ m), in which the ice can repeatedly interact with the seafloor as the water level rises and falls under the influence of winds and tides. This process can result in flexure fracturing of the ice surface, which can also lead to coherence loss. Similar observations of poor co-

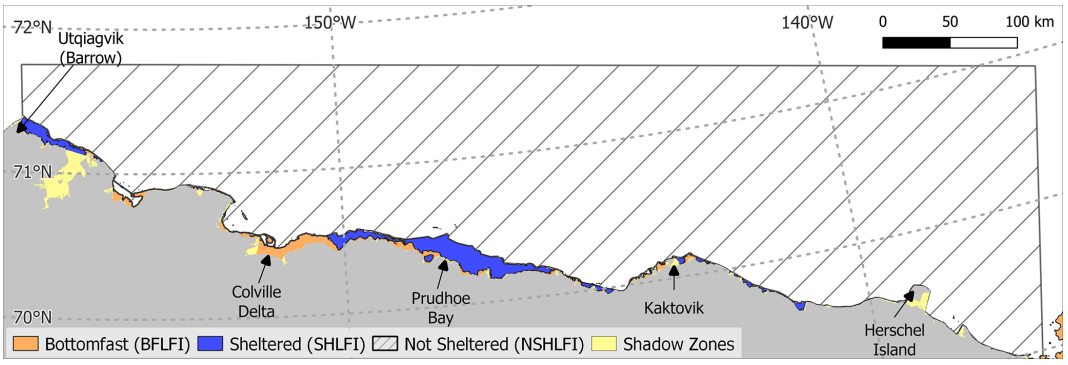

Figure 2. Spatial extent of the masks use for the derivation of the apparent strain thresholds associated with the stability zones from Dammann et al. (2019). Orange areas are bottomfast, blue is sheltered, and hashed black is not-sheltered. Yellow shaded regions represent "shadow regions" discussed in Sect. 2.2.

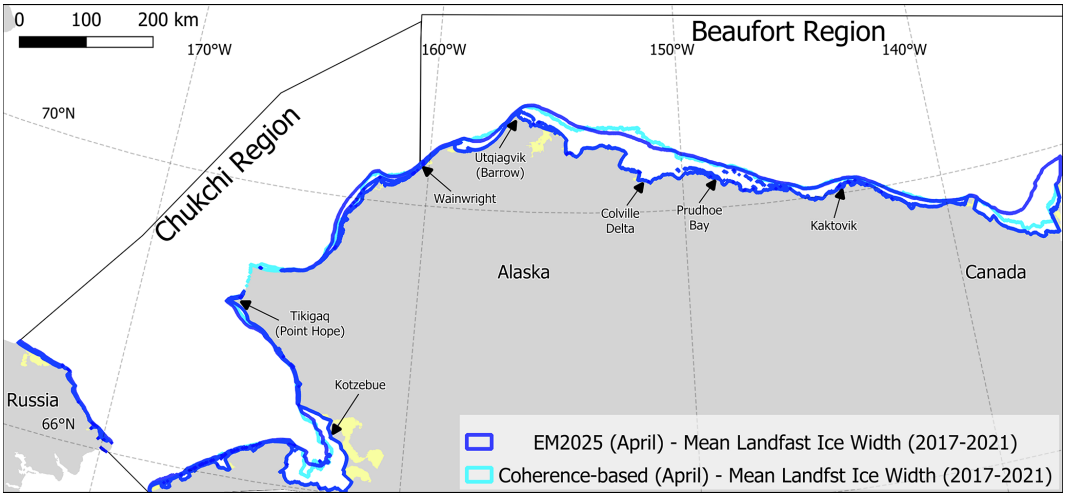

Figure 3. Spatial comparison of the April monthly mean (2017–2021) landfast ice width across the study region using the coherence based mosaics (cyan) and the EM2025 dataset (blue). Yellow regions are "shadow zones" where the coast vectors do not reach.

herence using C-band SAR over Kotzebue Sound were made by Dammann et al. (2019).

In the month of May (Fig. 4F), the landfast ice width difference between the two datasets is more consistently negative. In the Beaufort region, the coherence-based method measured on average 10.7 km less landfast ice extent during May. Similarly, in the Chukchi region the coherence method measured 5.4 km less landfast ice than the EM2025 dataset. The differences are due to extensive areas where no landfast ice was identified by the coherence-based method, but landfast ice was still present in both the Chukchi and Beaufort regions in the EM2025 dataset. In particular, Kotzebue Sound never met the coherence threshold to be considered landfast ice during May of any season from 2017–2021. Surface melting is the most likely cause of this underestimate and highlights the limitations of using coherence to identify landfast ice outside of the winter months.

3.2 Monthly mean apparent strain

Although there is considerable variability in monthly mean ϵ_a at the scale of adjacent pixels, there was an overall tendency for lower ϵ_a values to be found near the coast and higher values to occur closer to the SLIE (Figs. 5 and 6). This spatial distribution becomes more evident as the landfast ice season progresses and another tendency emerges in which the apparent strain in landfast ice tends to decrease over time (Fig. 7). Both Figs. 5 and 6 are representative of the mean seasonal progression of landfast ice extent and apparent strain values while Fig. 7 depicts how the monthly distribution evolves within the whole study region. The inset of each figure, denoted by a lowercase A, is a zoomed-in view near Utqiagvik, Alaska. Dark blue areas indicate very stable landfast ice low apparent strain, while yellow indicates relatively less stable landfast ice high apparent strain (Figs. 5 and 6). The transition from yellow to green to blue, high to low apparent strain, within Elson lagoon throughout the winter

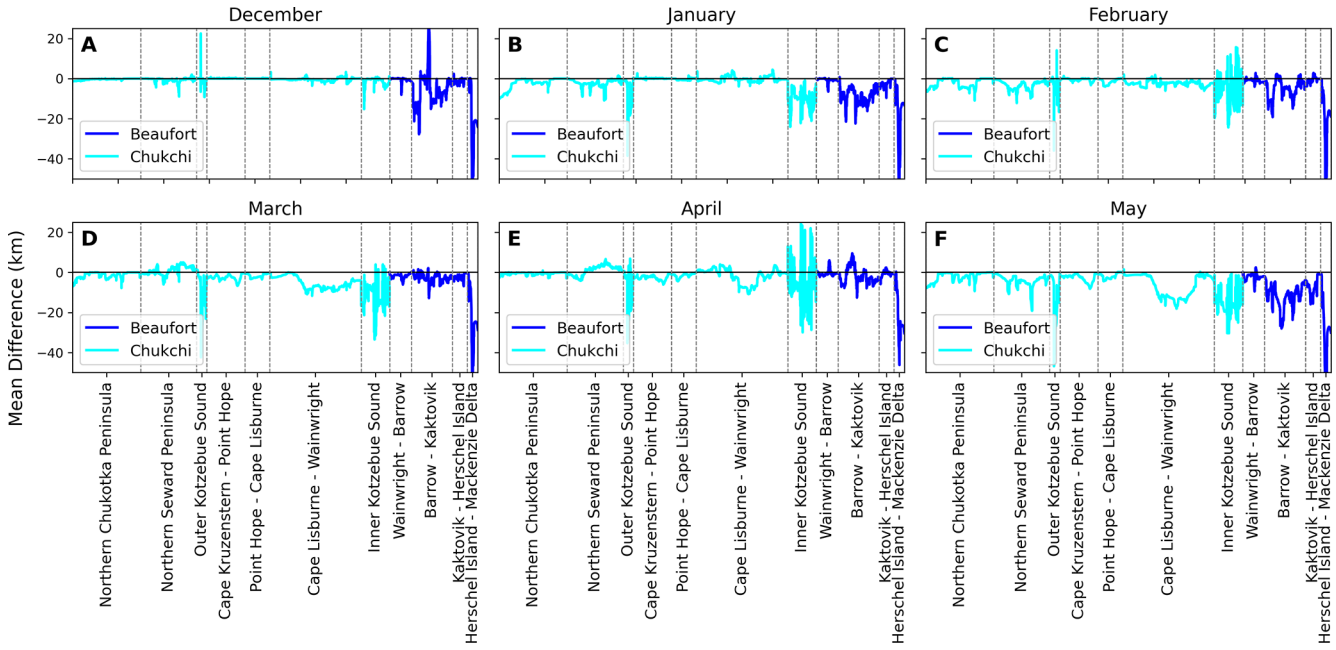

Figure 4. Difference of monthly average landfast ice width measured by the EM2025 dataset and the coherence-based method from 2017–2021 in December through May. Negative values indicate an under estimate by the coherence-based method. Cyan indicated the measurements occurred in the Chukchi region while blue is the Beaufort region. Vertical dashed gray lines indicate the bounds of the subregions shown in Fig. 1.

months indicates that stability increases as landfast ice persists (Figs. 5Aa–Ca and 6Aa–Ca). By calculating the probability distribution of monthly ϵ_a values, the modal value of ϵ_a decreases from December to May (Fig. 7). In addition, the distributions are right-skewed and the proportion of high apparent strain pixels decreases in the later months. Both of these changes result in a greater proportion of the landfast ice pixels having a lower apparent strain (i.e. more stable) during the later months of the season. During the month of May, very few pixels within the Chukchi region met the coherence threshold (Fig. 6C). In both regions, areas of landfast ice did not meet the coherence threshold to be considered landfast ice during the month of June, thus the distributions were omitted. The method performs robustly during the winter months, when landfast ice is most extensive and stable, and prior to the onset of surface melting.

3.3 Quantitative classification of landfast ice stability

In the Beaufort Sea, landfast ice typically reaches its seasonal maximum width during April (Mahoney et al., 2014). This is also the month for which Dammann et al. (2019) qualitatively defined landfast ice stability throughout the Arctic based on interferometric phase gradient. Hence, we use the monthly mean ϵ_a values for the month of April to derive the probability distributions of ϵ_a within the three stability zones identified in Fig. 2. The distributions of apparent strain in each stability zone bottomfast (orange), sheltered (blue), and not-sheltered (black) are shown in Fig. 8. The bottomfast region has a bimodal distribution while the sheltered and not-sheltered zones have well-defined and distinct modes. The modal apparent strain value in the bottomfast ice zone is the lowest while the not-sheltered zone has the highest. The bimodal distribution of apparent strain values within the bottomfast stability zone is likely associated with tide cracks, which form at the oceanward boundary of bottomfast ice. The distributions for sheltered and not-sheltered zones are approximately lognormal with considerable overlap which is expected, as we assume the not-sheltered zone contains landfast ice which is stabilized by grounded ridges. The overlap between the distribution of ϵ_a values within the SHLFI and NSHLFI reinforces the idea that landfast ice which is shoreward of a barrier island, sheltered, has a similar ϵ_a as landfast ice shoreward of a grounded ridge (stabilized). In addition, the wider distribution apparent strain of the NSHLFI compared to the SHLFI is further evidence of multiple stability classes being present within the NSHLFI area.

To separate these stability classes objectively, we used Otsu's algorithm (Otsu, 1979) to determine ϵ_a thresholds for each class. Physically, the stability classes represent landfast ice which has similar regimes to the stability zones defined by Dammann et al. (2019). Bottomfast ice is broadly in contact with the seafloor (resting or frozen), stabilized ice is shoreward of a point feature (either barrier island or grounded ridge), and nonstabilized represents the floating extension which only has a point feature shoreward of its lo-

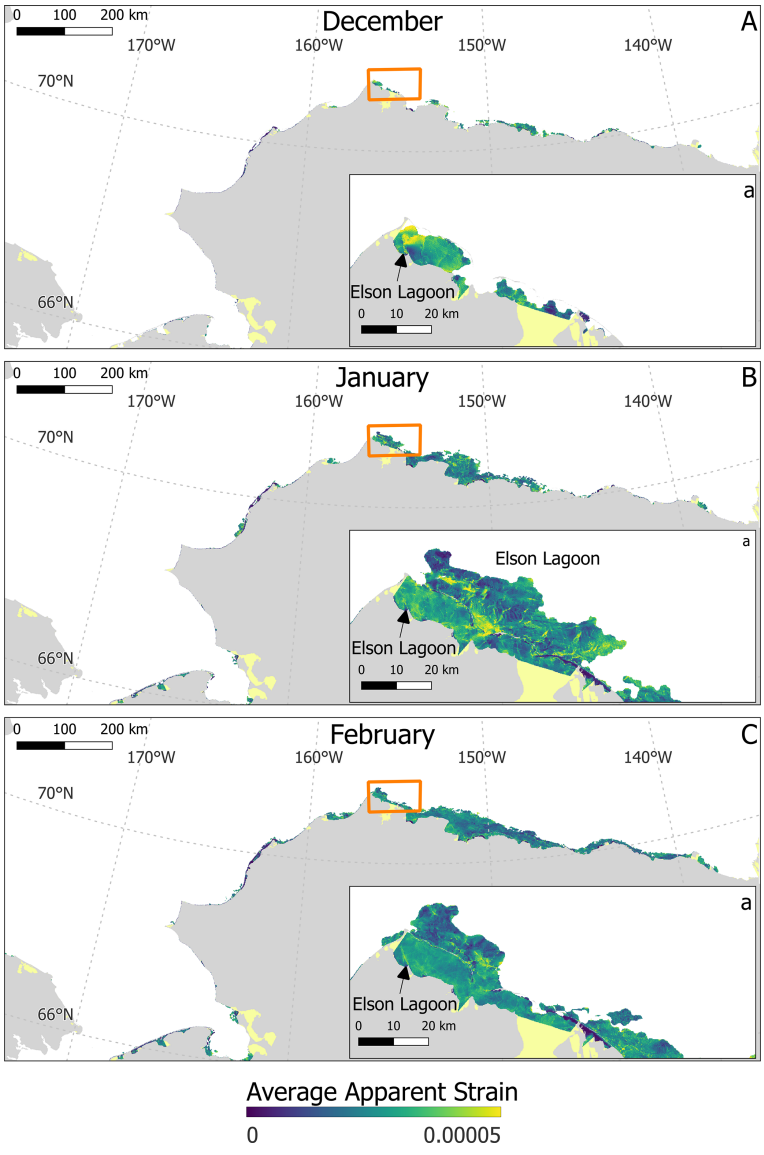

Figure 5. Monthly mean apparent strain values for December **(A)**, January **(B)**, and February **(C)** for both Beaufort and Chukchi regions from 2017–2021. The orange box denotes the extent of inset figure in each **(a)**. Dark blue areas mark low apparent strain regions while yellow denotes high apparent strain.

cation. The apparent strain threshold for the bottomfast ice stability class was determined to be $\epsilon_a = 8.6 \times 10^{-6}$, marked by a yellow dashed line in Fig. 8. For the sheltered and not-sheltered classes, the thresholds were determined to be $\epsilon_a = 1.8 \times 10^{-5}$ and $\epsilon_a = 2.4 \times 10^{-5}$ marked by blue and black dashed lines, respectively (Fig. 8). We chose the threshold of the sheltered class to differentiate the sheltered class from the not-sheltered class. This was done since we assumed that stabilized landfast ice exists within the not-sheltered region, landfast ice that is stabilized by grounded ridges. Furthermore, we assumed the apparent strain values of landfast ice which is stabilized by barrier islands and grounded ridges are similar. Determining thresholds using Otsu's method yielded two objectively determined thresholds that define the apparent strain bounds for our three stability classes:

1. Bottomfast: $\epsilon_a \leq 8.6 \times 10^{-6}$
2. Stabilized: $8.6 \times 10^{-6} < \epsilon_a \leq 2.4 \times 10^{-5}$
3. Nonstabilized: $\epsilon_a > 2.4 \times 10^{-5}$

To test our apparent strain thresholds, we calculated the apparent strain of the interferograms used by Dammann et al. (2019) along the Beaufort coastline and compared the extents of our quantitatively defined stability classes to their qualitative stability zones. Apart from the method of stability classification, qualitative vs. quantitative, Dammann et al. (2019)

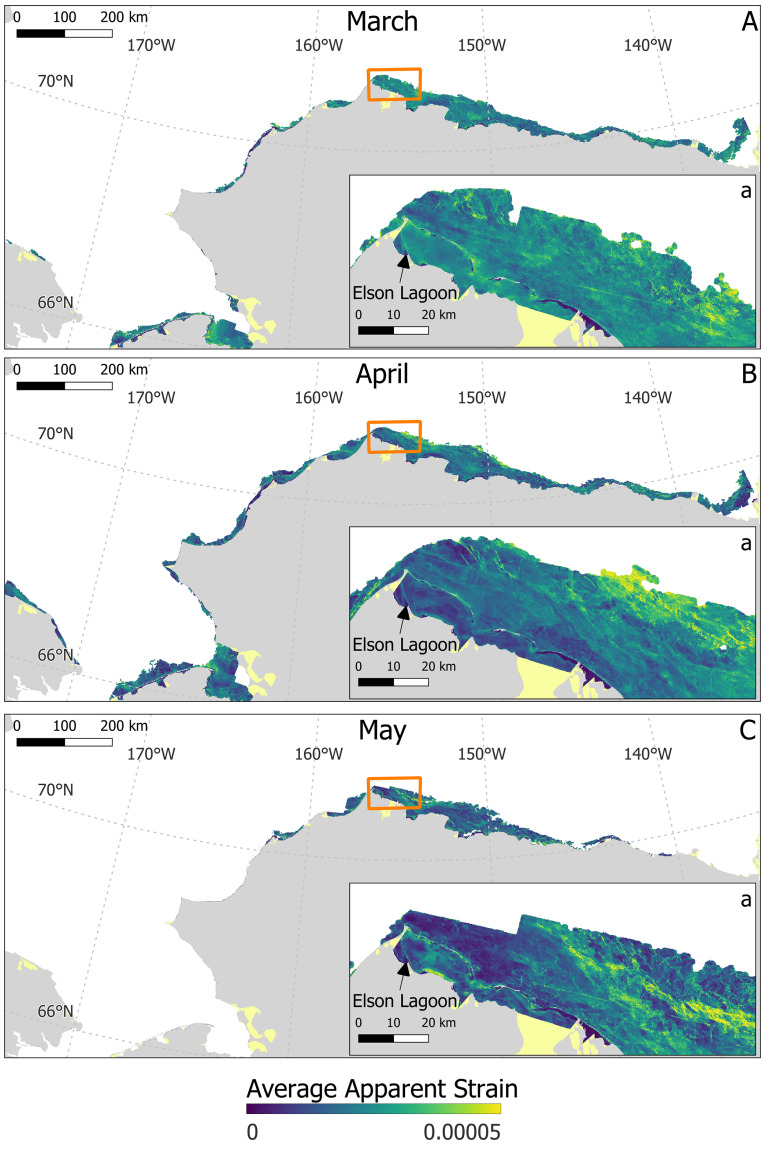

Figure 6. Monthly mean apparent strain values for March **(A)**, April **(B)**, and May **(C)** for both Beaufort and Chukchi regions from 2017–2021. The orange box denotes the extent of inset figure in each **(a)**. Dark blue areas mark low apparent strain regions while yellow denotes high apparent strain.

did not enforce a strict temporal baseline for the SAR pairs, and they used a non-zero coherence value to identify the seaward landfast ice edge (SLIE). The three Sentinel-1 SAR pairs used by Dammann et al. (2019) were: 8 April 2017–2 May 2017; 15 April 2017–9 May 2017; and 17–29 April 2017. The interferograms produced from these SAR pairs and the resulting apparent strain maps can be seen in Fig. 9A and B. The interferograms show the extents of the stability zones defined by Dammann et al. (2019) with the areas outlined in red and identified as bottomfast, purple stabilized and cyan nonstabilized (Fig. 9A). The apparent strain values were sorted into the stability classes such that we could directly compare the extent of the qualitative zones and the quantitative classes (Fig. 9C). The main difference between the methods is the extent of the nonstabilized landfast ice. The higher coherence threshold used in this study, $\gamma \geq 0.3$, compared to the non-zero requirement by Dammann et al. (2019), resulted in an underestimate of landfast ice extent. However, the transition from stabilized to nonstabilized is captured well (Fig. 9Ca). In addition, the areas that are classed as bottomfast are separated from nearby stabilized landfast ice by a thin area of nonstabilized ice. It is likely these areas of high apparent strain are associated with tide cracks due to the geometry and location.

To further investigate the performance of the apparent strain thresholds, we produced a confusion matrix of the clas-

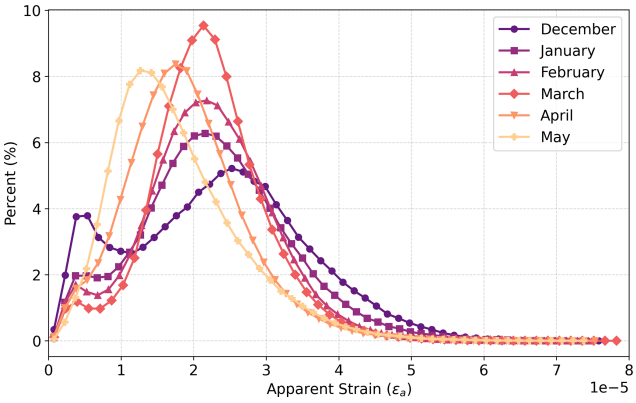

Figure 7. Distribution of the monthly mean apparent strain values from December through May for all pixels within the study region from 2017–2021.

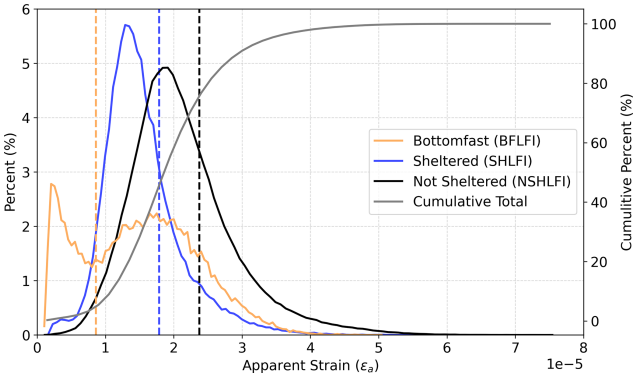

Figure 8. Distribution of the average apparent strain values from April 2017–2021 in each stability zone defined in Fig. 2 (solid lines). Dashed lines indicate the value of the Otsu threshold for each stability zone.

sification types by Dammann et al. (2019) vs. this study's apparent strain classes (Table 1). The nonstabilized class is the only class where both methods agreed on the majority of pixels which met the ≥ 0.3 coherence threshold (Table 1). It is likely the classification disagreement, where the apparent strain indicated bottomfast ice while Dammann et al. (2019) concluded that stabilized is the result of multiple grounded ridges in a small area. Both regions of large misclassifications, west of the Colville Delta and north of Prudhoe Bay (Fig. 9C), have been identified as common areas for grounded ridges (Lange et al., 2025). Thus we do not view the disagreement of classification as wrong, just that there are various processes that can reduce apparent strain, and in the right conditions, produce very stable landfast ice.

Table 1. Percentages of landfast ice classification types the based on qualitative characteristics by Dammann et al. (2019) and apparent strain thresholds for SAR pairs displayed in Fig. 9A.

	Apparent Strain Class		
Dammann et al. Class	Bottomfast	Stabilized	Nonstabilized
Bottomfast	41.8	33.4	24.8
Stabilized	28.1	46.6	25.3
Nonstabilized	3.6	22.8	73.6

4 Discussion

4.1 Suitability of InSAR for routine identification of landfast sea ice

In general, landfast ice extent is captured well using interferometric coherence during the winter months of the landfast ice season but under-identifies landfast ice extent at the beginning or end of the season. Despite the typical presence of landfast ice in both the Chukchi and Beaufort regions during November and June (Mahoney et al., 2024; Mahoney and Einhorn, 2026), we did not find any pixels outside the land mask with coherence values ≥ 0.3 until December or after May. The coherence-based method does not capture landfast ice extent during the beginning and end of the landfast ice season, two important parts of the season when discussing changes between seasons. In the early winter, the loss of coherence over immobile landfast ice is likely caused by the rapid changes in the dielectric properties of the ice surface that occurred during the early stages of growth (e.g. Winebrenner et al., 1996). During the months of December and January, the average monthly width of landfast ice identified by our coherence-based method under represents relative to the EM2025 dataset from 2017–2021 (-5.1 km in the Beaufort and -0.5 km in the Chukchi). Much of the difference in the Beaufort region occurs between Point Barrow and Kaktovik where our InSAR-derived results show the landfast ice is consistently 6–10 km narrower. In the Chukchi region, differences between the InSAR-derived width and EM2025 monthly mean width occur primarily in Kotzebue Sound. Similar to the area between Point Barrow and Kaktovik in the Beaufort region, the InSAR-derived width was on average 8.2 km lower than the EM2025 width in Kotzebue Sound during January.

Agreement between InSAR-derived landfast ice extent and the EM2025 dataset is best from February through April. The InSAR-based method still slightly underestimated landfast ice width compared to the EM2025 dataset by an average of 2.5 and 4.4 km, for the combined Chukchi and Beaufort regions from February through April. During these months, there are areas where the coherence-based method overestimated the landfast ice extent. Specifically, during April north of the Colville Delta (Fig. 3) the coherence-based SLIE is

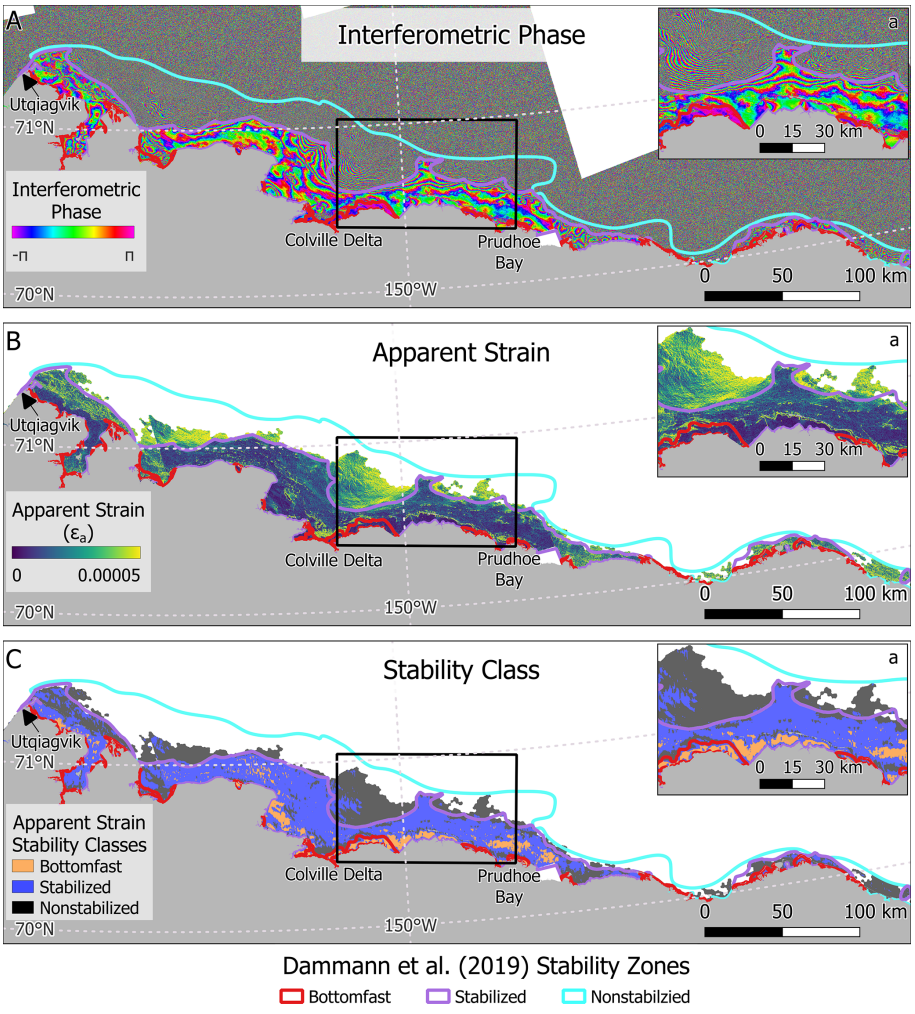

Figure 9. Spatial representation of the interferogram **(A)**, apparent strain **(B)**, and apparent strain derived stability classes **(C)** compared to the stability zones defined by Dammann et al. (2019) using the same SAR pairs. The black box indicates the location of the inset **(a)**.

1–2 km further offshore than the EM2025 dataset. This is an area identified as a node (Mahoney et al., 2014) and in proximity to grounded ridges (Lange et al., 2025). Finally, in May, the InSAR-based method underestimated the landfast ice width consistently across the study region. The consistent under measuring of landfast ice in May is attributed to surface melting causing a loss of coherence between acquisitions. Overall, the coherence-based identification of landfast ice measures the landfast ice width well, however there are certain areas where the combination of 12 d between acquisitions and C-band SAR prevents the methods from identifying landfast ice. On this basis, we find that 12 d repeat Sentinel-1 InSAR may be a useful tool for helping discriminate landfast ice extent during the coldest months of the year when the dielectric properties of the ice surface are most stable. With the imminent launch of the NISAR satellite, the combination of a 12 d repeat orbit with a L-Band sensor will likely improve the retention of coherence over landfast ice in the Arctic. In addition, NISAR might allow for coherence to be maintained over Antarctic landfast ice, something C-band is unable to do on a 12 d repeat orbit. Meyer et al. (2011) showed that L-band coherence could be maintained for 45 d over landfast ice and so we anticipate that NISAR expands the useful window of this method for a greater portion of the landfast ice season.

4.2 Regional variability and annual evolution of landfast ice stability

We have shown that, over the study area, the distribution of apparent strain evolves such that the modal value of ϵ_a decreases monotonically from December to May across the whole study region (Fig. 7). This pattern suggests that landfast ice becomes more stable the longer it remains in place over winter. To better understand the processes likely to be responsible for this, we partitioned this analysis among the 11 subregions shown in Fig. 1 and calculated the distribution of monthly mean apparent strain in each subregion (Fig. 10).

Similar to the study region as a whole, the mode of the apparent strain distribution decreases monotonically from month to month, with landfast ice transitioning toward more stable categories over time in most subregions (Fig. 10). Subregion 9 (Point Barrow to Kaktovik) (Fig. 10), is the best representation of the evolution of apparent strain in a subregion throughout the year due to the large extent amount of landfast ice and the variety of coastlines. It should be noted that, from December to April, this increase in stability occurs, while the overall extent of landfast ice also increases, suggesting that the process by which the SLIE advances also increases the stability of the landfast ice. In some subregions, the total landfast ice extent in May is less than that in April, so any increase in the modal ϵ_a value between these two months likely indicates that the least stable landfast ice is the first to detach. However, not all subregions follow a general decrease in apparent strain throughout the season.

Subregions with extensive lagoon systems have different trends of apparent strain distributions throughout the season. Subregion 1 (Northern Chukotka Peninsula), Subregion 2 (Northern Seward Peninsula), and Subregion 7 (Point Hope to Wainwright) are regions where the coastline is primarily composed of lagoons. The landfast ice within these lagoons forms prior to that formed outside of the lagoons. During the months when fast ice only exists within a lagoon, the distribution indicates a lower apparent strain mode. In this instance, all the landfast ice is being stabilized by the barrier islands, and depending on the depth of the water and the thickness of the ice, it could be bottomfast. The distribution of apparent strain within Subregion 7 (Fig. 10G), is a prime example of the distribution in a subregion dominated by lagoons. The monthly distributions are concentrated within the bottomfast class in the early months (December–February), then follow a typical seasonal progression in March through May (Fig. 10G). The high percentage of low apparent strain values in Subregion 7 during the early months is due to the landfast ice not existing outside of shallow lagoons (Fig. 5A–C). It is not until March when substantial amounts of landfast ice exist outside of the shallow lagoons.

4.3 Identification of abrupt increases in apparent strain associated with grounded features

We have shown that the three apparent strain classes we defined in Sect. 3.3 for bottomfast, stabilized, and nonstabilized landfast ice align well with the extent of equivalent stability zones identified qualitatively by Dammann et al. (2019) from single interferograms. Within other single-interferogram apparent strain maps, we commonly observe strong gradients in apparent strain that are not evident in the monthly average maps. These strong gradients are likely associated with the transition from grounded to floating landfast ice. For example, at the seaward edge of the bottomfast ice, there are tide crack zones where the floating landfast ice flexes in response to sea level variations while the bottomfast ice remains stationary. The difference in vertical motion across this narrow region (typically tens of meters wide) leads to a region of high fringe density, like those found at the grounding lines of ice shelves and tidewater glaciers (Friedl et al., 2019), resulting in high apparent strain. Examples of such features can be seen in two apparent strain maps from 5–17 April 2017 (Fig. 11A) and 9–21 April 2022 (Fig. 11B) near Oliktok Point in the Beaufort region. We see abrupt increases of apparent strain in both maps associated with a tide crack, a barrier island, and a grounded ridge (Fig. 11C). During 2022, the landfast ice was more extensive allowing for the formation of a second grounded ridge (Fig. 11C). The resemblance of these features to those around barrier islands leads us to identify them as the tide crack zone around grounded ridges. Moreover, they occur at the locations grounded ridges have been identified in this region during the 2021–2022 landfast ice season by Lange et al. (2025). In addition, similar patterns in apparent strain values can be observed within the lagoon and oceanward of the barrier island, providing further evidence the abrupt gradient in apparent strain is associated with a stabilizing feature.

The shoreward feature identified as a grounded ridge occurred in approximately the same location in both 2017 and 2022, but the apparent strain pattern deviates offshore of this location by around 23 km. Both transects indicate a reduction of apparent strain offshore of the seaward grounded ridge (Fig. 11C). We believe this to be the local stabilized effect of a grounded feature. However, proving and interpreting this is outside the scope of this study. It is also possible the areas of high apparent strain gradients are not the grounded features, but the low apparent strain features surrounding these areas. A direct comparison to the location of the grounded ridges by Lange et al. (2025) could provide evidence of the apparent strain pattern related to the grounded features vs. the fast ice surrounding the ridge.

5 Conclusions

InSAR-based methods hold great promise for improving our understanding of both the spatial extent of landfast sea ice and its relative stability. Meyer et al. (2011) already demonstrated the usefulness of interferometric coherence in delineating landfast ice from the mobile pack ice using 45 d repeat L-band PALSAR data. Our investigation shows that a similar approach with a coherence threshold for C-band can work well during the winter months and throughout most of our study area using 12 d C-band Sentinel-1 data. During the winter months, February–April, landfast ice widths derived from the coherence threshold approach typically agreed to within a few kilometers of those derived from the EM2025 dataset (Fig. 4C–E). However, factors unrelated to the motion of the ice reduce coherence at the beginning and end of the season, occasionally resulting in false absence of landfast ice (corresponding to a 100 % underestimate in Fig. 4E and

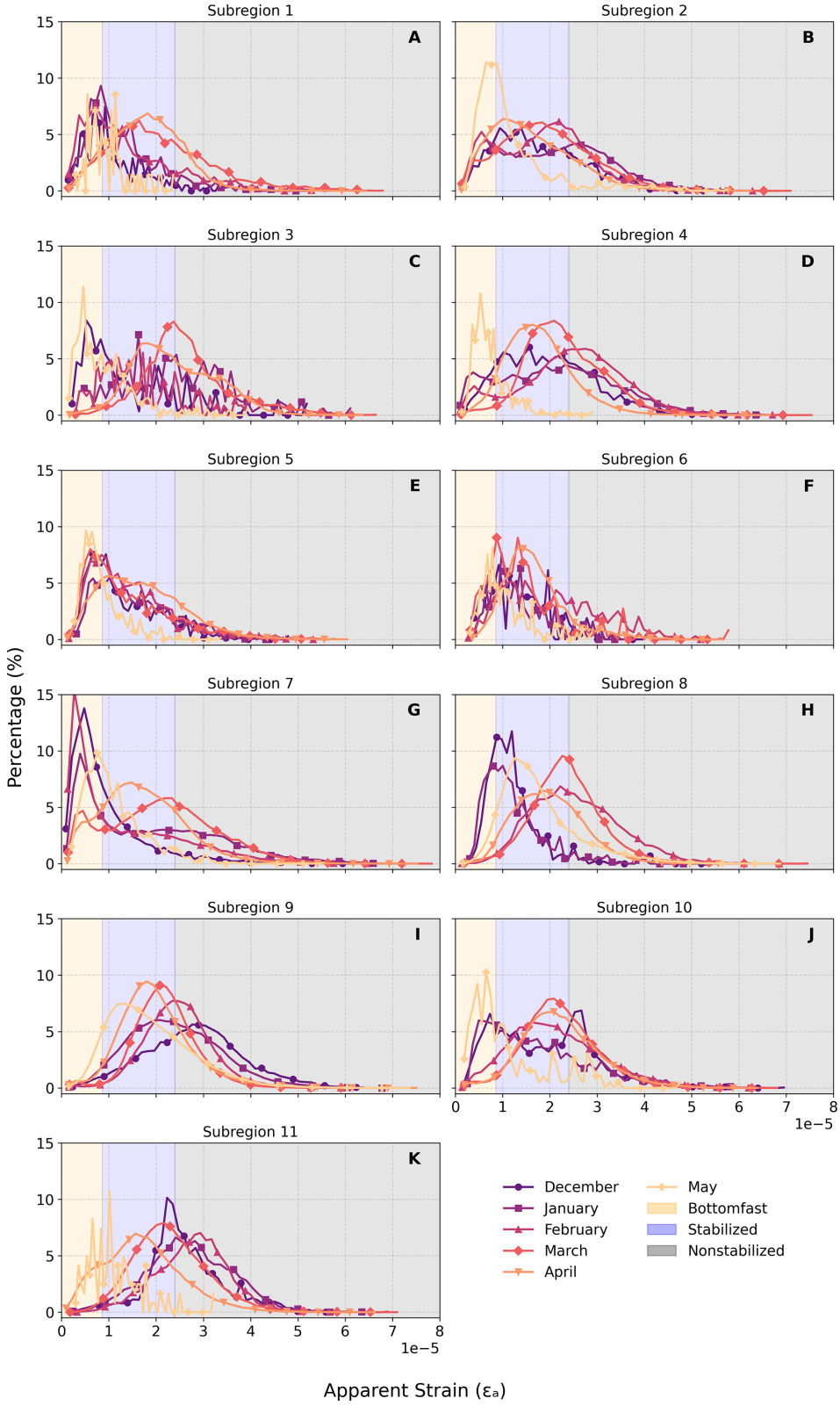

Figure 10. Distributions of monthly apparent strain in the 11 subregions described in Fig. 1. Each month from December through May is represented by lines which progress from purple to yellow. Shaded regions indicate the apparent strain values associated with each stability class: orange is bottomfast, blue is stabilized, and gray is nonstabilized.

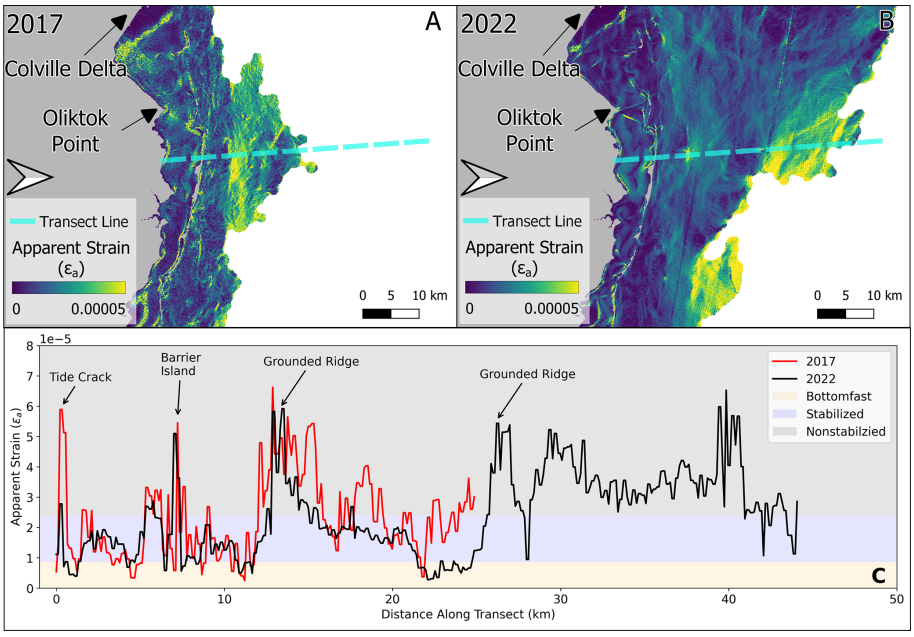

Figure 11. Apparent strain maps from April 2017 **(A)** and April 2022 **(B)** and the associated apparent strain values along a transect near Oliktok Point, Alaska **(C)**. Apparent strain values along each transect (2017 red, and 2022 black) can be sorted into stability classes and used to identify the location of features.

F, for example). Hence, the usefulness of our interferometric coherence method for identifying landfast ice would be improved with either a shorter period between SAR images or use of a longer radar wavelength. We therefore look forward to the launch of the NASA–ISRO synthetic aperture radar (NISAR) currently scheduled to launch in 2025. The L-band sensor and 12 d repeat interval should open new opportunities for routine mapping of landfast extent using InSAR.

In a quantitative expansion the work done by Dammann et al. (2019), we find apparent strain, ϵ_a, can serve as a meaningful measure of landfast ice stability. Specifically, we find that the distributions of ϵ_a values within the bottomfast ice zone and either seaward or shoreward of barrier islands have distinct modes. This allows us to define three landfast ice stability classes on the basis of apparent strain: bottomfast ice ($\epsilon_a \leq 8.6 \times 10^{-6}$), stabilized ($8.6 \times 10^{-6} < \epsilon_a \leq 2.4 \times 10^{-5}$), and nonstabilized ($\epsilon_a > 2.4 \times 10^{-5}$). Single interferograms indicate a spatially abrupt change in apparent strain between the stabilized and nonstabilized landfast ice. These abrupt changes are not present within the monthly average apparent strain images (Figs. 5 and 6). The grounded ridges likely persist between interferograms in the same season. However, they are not present in the monthly averages, indicating that the strain field in landfast ice evolves more rapidly than the repeat interval of Sentinel-1 and because the monthly averages combine results from different viewing geometries. Nonetheless, the boundary between stabilized and nonstabilized ice is often associated with features that we interpret to be grounded features (Fig. 11), which suggests our classification represents physical differences in the strain experienced by landfast ice on either side. To our knowledge, this is the first time InSAR has been used to identify individual grounded ridges based on localized values of high apparent strain. Our deduction that these high apparent strain points are grounded ridged is strongly supported by matching the locations of grounded ridges identified by Lange et al. (2025), based on ICESat-2 altimetry data. Moreover, our observations support their findings that grounded ridges are commonly located shoreward of the landfast ice edge.

Along with the establishment of the apparent strain thresholds we defined, we observed a decrease in apparent strain throughout the season. The increase in stability the longer the landfast ice persists is likely due to thickening, but further investigation into the cause is needed. A fundamental flaw in using information derived from interferometry is the inability of InSAR to capture along-track deformation. Being limited to the magnitude of line-of-sight deformation causes an under representation of the total possible deformation that occurred. Implementing methods to resolve the two-dimensional strain, demonstrated by Fedders et al. (2024), would improve our ability to classify landfast ice stability based on the apparent strain. The ability of InSAR to identify these areas of varying stability can hold immense value to members of Arctic coastal communities allowing them to continue to utilize on the landfast ice safely.

Appendix A: Coherence Threshold Derivation

Derivation of the C-Band coherence threshold to delineate landfast ice from mobile pack ice was done using SAR pairs acquired in both the Chukchi and Beaufort regions, throughout the winter to ensure the threshold was applicable to all SAR pairs used in this study. Landfast ice has been identified using a simple coherence threshold (Meyer et al., 2011). However, due to the increased sensitivity and resulting reduction of coherence associated with a shorter wavelength, the 0.1 threshold established by Meyer et al. (2011) using L-Band is not applicable to SAR pairs acquired using a C-Band SAR. Thus we needed to establish a coherence threshold to identify landfast ice using C-Band. We selected 2 reference scenes, one from the Chukchi region and one from the Beaufort and SAR pairs occurring in each month from December through June. The Chukchi reference scene is located on the north coast of the Seward Peninsula, covering most of the area denoted as Subregion 2 in Fig. 1. The Beaufort reference scene is located about Barrow Alaska and primarily located in Subregion 9 (Fig. 1). While both primary and secondary acquisitions do not always occur in the month assigned, these were the SAR pairs available which fit our spatial and temporal baseline criteria, detailed in Sect. 2.3. Details about the SAR pairs used for each month can be found in Table A1. We used each normalized coherence image produced by the HyP3 processing Hogenson et al. (2016) to derived the best coherence threshold for landfast ice using C-band.

Delineating landfast ice from mobile pack ice can be accomplished by applying a threshold to the coherence image, then applying morphological filtering to remove spurious offshore areas being identified as landfast ice. Prior to the testing of different coherence thresholds we computed the monthly minimum landfast ice extent in each month for the 2017–2018 season using the EM2025 dataset to represent the true fast ice extent. The minium landfast ice extent was chosen as coherence is only maintained if the landfast ice does not breakout over the entire 12 d orbit. In addition, new landfast ice formed between the acquisition dates would not present as coherent. Thus we found it appropriate to use the monthly minimum landfast ice extent measured by the EM2025 dataset as a comparison. The pixels shoreward of the monthly minimum landfast ice extent were treated as fast ice, and pixels outside were treated as not landfast ice. To maintain consistent window sizes with the phase gradient calculation, Sect. 2.4 we applied a 4 pixel smoothing filter to the coherence images. An example of a normalized coherence image can be seen in Fig. A1. The SAR pair is the same used in Fig. A3H. The pixels from each normalize coherence images were then sorted into areas identified as landfast ice or not landfast ice by the EM2025 monthly minimum. The distribution of normalized coherence values for areas identified as landfast ice (solid) and not landfast ice (dashed) in the corresponding month can be seen in Fig. A2. In both regions, the areas identified as not fast ice peak around 0.2. This is in contrast to the areas identified as landfast ice which are more evenly distributed across higher coherence values or having peaks above 0.8. In the Chukchi (December, January, and June) and Beaufort (June), the distribution of coherence is similar to the not landfast ice areas (Fig. A2A and B). We suspect the reduction in coherence in the early months is due to inherent bias when using active microwave remote sensing over growing sea ice while in June we suspect surface melting to cause the coherence distribution to be similar to not landfast ice. Figure A2 confirms the coherence threshold for established by Meyer et al. (2011) of 0.1 using L-Band is not directly transferable to C-band.

To derive the C-Band coherence threshold for identifying landfast ice, we used a systematic approach by applying different thresholds from 0.01 to 1, increasing in 0.01 increments, and computing a confusion matrix for each month. The categories of the confusion matrices were: Correct landfast ice (EM2025 landfast ice, coherence landfast ice) actually landfast ice but predicted not landfast ice (EM2025 landfast ice, coherence not landfast ice) not landfast ice but predicted landfast ice (EM2025 not landfast ice, coherence landfast ice) and correct not landfast ice (EM2025 not landfast ice, coherence not landfast ice). We then calculated the threshold with the highest percentage of correctly identified landfast ice pixels and correctly identified not landfast ice pixel for each month in each sector. However, due to a high percentage of the pixels being classed as not fast ice, we found the best thresholds identified had higher thresholds as this method favored true negatives more than true positives. To account for the imbalance in true negatives and true positives we weighted the accuracy of each threshold. Then we used the weighted accuracies determined the best coherence threshold in each sector and month, summarized in (Table A2). Based on the distribution of these best thresholds for each month and the previous knowledge there are SAR pairs which struggled to retain coherence due to suspected thin ice and melting, Chukchi (December, January, and June) and Beaufort (June) we chose 0.3 as the coherence threshold to identify landfast ice with C-Band.

The 0.3 coherence threshold was then applied to the 14 SAR pairs A1 to confirm the coherence method captured the spatial pattern of landfast ice in the Chukchi and Beaufort regions. Similar to the derivation of the threshold we compared the spatial extent of the landfast ice identified by the coherence method to the minimum extent measured by the associated month during the 2017–2018 season from the EM2025 dataset. Areas which both methods identified landfast ice colored green, false positives are dark orange, false negatives are light orange, and cyan areas are areas both methods identified as not landfast ice (Fig. A3). In both regions, the coherence method over estimates the monthly fast ice minimum extent and under estimates in the latter half, expectantly in the Beaufort region. We included the monthly maximum extent, denoted by the black line in each panel of Fig. A3 as a way to show the range of landfast ice extent during each month

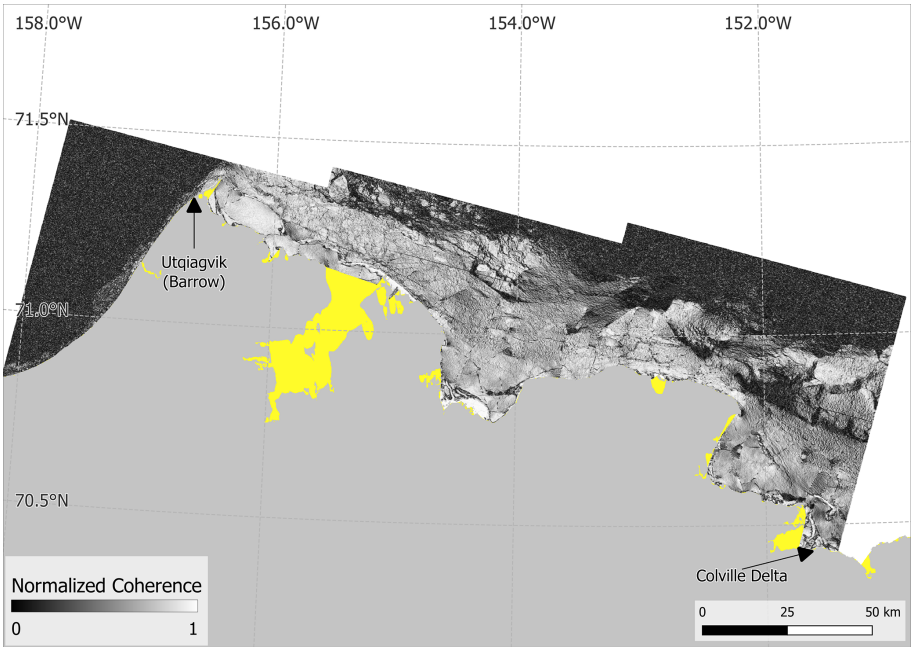

Figure A1. Example of a normalize coherence image from SAR pairs 11 and 23 March 2018. Black indicates low coherence while white indicates high coherence. Yellow regions are shadow regions.

Table A1. Acquisition dates of Sentinel-1 SAR pairs used for the derivation the the coherence threshold.

Primary Acquisition Date	Secondary Acquisition Date	Region	Month Assigned
13 December 2017	25 December 2017	Chukchi	December
18 January 2018	30 January 2018		January
11 February 2018	23 February 2018		February
31 March 2018	12 April 2018		March
12 April 2018	24 April 2018		April
18 May 2018	30 May 2018		May
11 June 2018	23 June 2018		June
17 December 2017	29 December 2017	Beaufort	December
22 January 2018	3 February 2018		January
3 February 2018	15 February 2018		February
11 March 2018	23 March 2018		March
4 April 2018	16 April 2018		April
28 April 2018	10 May 2018		May
3 June 2018	15 June 2018		June

since the minimum landfast ice might not have occurred between SAR acquisitions. During June in the Beaufort region (Fig. A3N) the coherence method identified no fast ice. This is due to surface melting confirmed by the presence of melt pond from MODIS imagery.

Table A2. Best coherence threshold identified in each month and sector. And the percentage of pixels which the coherence method agreed with the EM2025 classification.

Month	Region	Threshold	Percentage Correct (%)
December	Chukchi	0.27	58
January		0.31	60
February		0.30	81
March		0.35	92
April		0.35	96
May		0.30	60
June		0.26	59
December	Beaufort	0.29	77
January		0.50	86
February		0.35	83
March		0.37	80
April		0.35	80
May		0.36	84
June		0.17	51

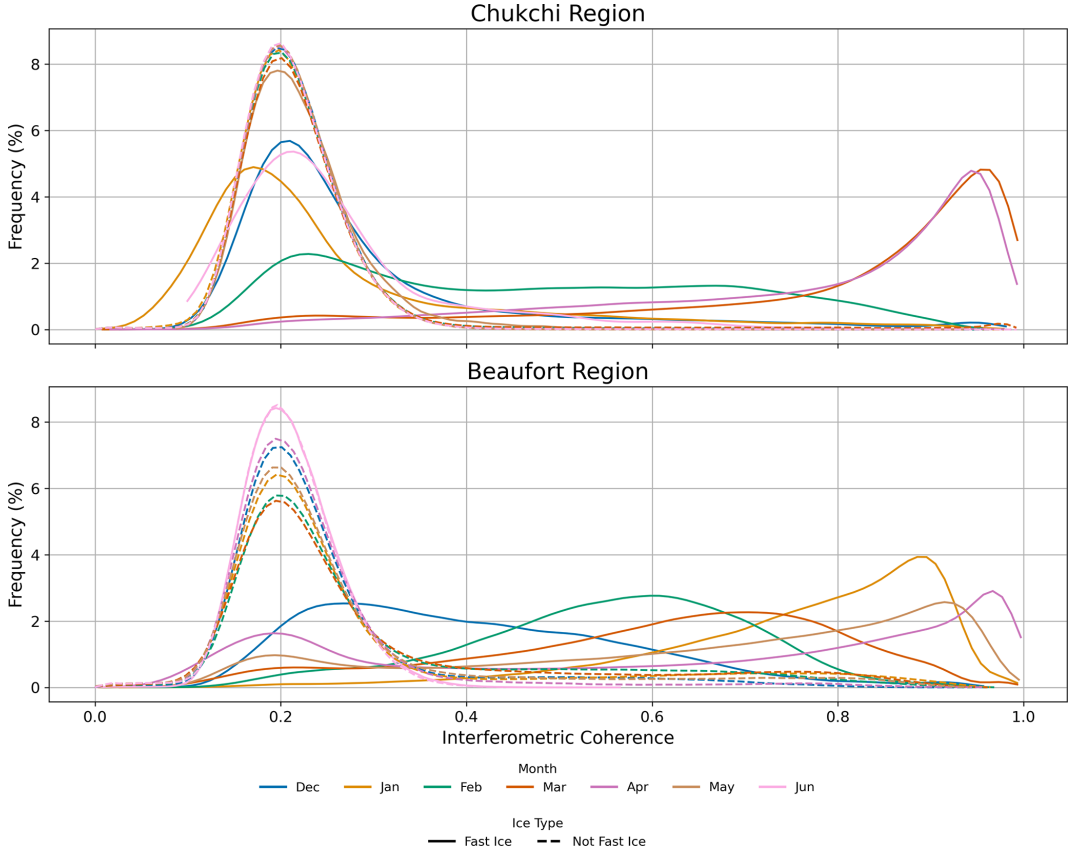

Figure A2. The distribution of normalized coherence values from SAR pairs acquired during each month from December through June of the 2017–2018 landfast ice season in the Chukchi and Beaufort regions. Monthly coherence distributions: solid lines show areas identified as landfast ice by EM2025, dashed lines show areas not identified as landfast ice.

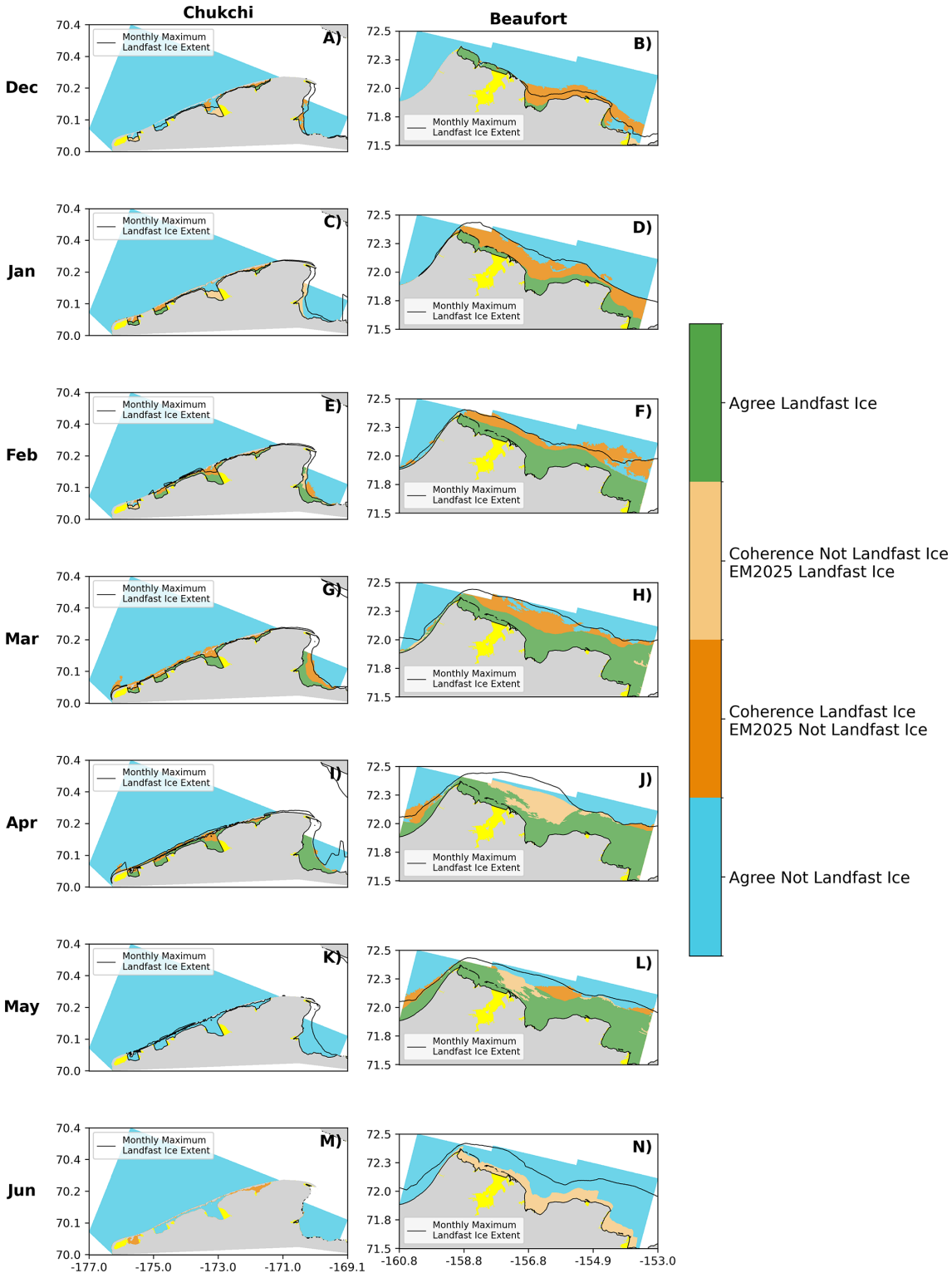

Figure A3. Spatial representation of the confusion matrix comparing the identification of landfast ice for each month and sector when using a 0.3 coherence threshold and monthly minimum extent from the EM2025 dataset during the 2017–2018 season. Yellow regions are shadow regions (Sect. 2.3).

Code availability. Code for processing of the ASF Vertex outputs into apparent strain can be found here (https://github.com/aheinhorn/Alaska_InSAR_CODE, last access: 14 June 2026 and https://doi.org/10.5281/zenodo.20692753, Einhorn, 2026). All the code for analyzing the fast ice extent of the coherence derived width and EM2025 derived width can be found here (https://github.com/armahoney/SLIEalyzer, last access: 14 JUne 2026 and https://doi.org/10.5281/zenodo.17353613, Mahoney, 2025)

Data availability. Sentinel-1 SAR imagery are openly accessible at the Alaska Satellite Facility' s Vertex tool (https://search.asf.alaska.edu/, last access: 14 June 2026), where users can search for imagery, request on-demand processing (include InSAR products), and download data. Registration with NASA EarthData is required but is open to anyone. The EM2025 dataset is available through the University of Alaska Fairbanks Scenarios Network for Alaska and Arctic Planning at https://catalog.snap.uaf.edu/geonetwork/srv/eng/catalog.search#/metadata/a6323019-0023-4e0d-98dc-a01b13bb7114 (last access: 14 June 2026) (for the Chukchi region) and https://catalog.snap.uaf.edu/geonetwork/srv/eng/catalog.search#/metadata/5adee563-786d-4b54-bbec-56dea055ec9a (last access: 14 June 2026) (for the Beaufort region) under a Creative Commons license (CC-BY 4.0).

Author contributions. All authors edited the manuscript. AE led the analysis, produced figures, and drafted the article. AM created the SLIEalizer package and provided scientific and editorial feedback and direction to the project.

Competing interests. The contact author has declared that neither of the authors has any competing interests.

Disclaimer. Publisher's note: Copernicus Publications remains neutral with regard to jurisdictional claims made in the text, published maps, institutional affiliations, or any other geographical representation in this paper. The authors bear the ultimate responsibility for providing appropriate place names. Views expressed in the text are those of the authors and do not necessarily reflect the views of the publisher.

Acknowledgements. Study collaboration and funding were provided by the US Department of the Interior, Bureau of Ocean Energy Management (BOEM), Environmental Studies Program, Washington, DC, under Agreement Number M19AC00021. We are also extremely grateful to the members of our Science Review Board, Hajo Eicken, Andrew Roberts, and John Walsh Study collaboration and funding were provided by the US Department of the Interior, Bureau of Ocean Energy Management (BOEM), Environmental Studies Program, Washington, DC, under Agreement Number M19AC00021

Financial support. This research has been supported by the Bureau of Ocean Energy Management (grant no. M19AC00021).

Review statement. This paper was edited by Ted Maksym and reviewed by three anonymous referees.

References

Bamler, R. and Hartl, P.: Synthetic aperture radar interferometry, Inverse Problems, https://doi.org/10.1088/0266-5611/14/4/001, 1998.

Barry, R. G., Moritz, R. E., and Rogers, J. C.: The fast ice regimes of the Beaufort and Chukchi Sea coasts, Alaska, Cold Reg. Sci. Technol., 1, https://doi.org/10.1016/0165-232X(79)90006-5, 1979.

Bieniek, P. A., Eicken, H., Jin, M., Mahoney, A. R., Jones, J., and Bhatt, U. S.: Seasonal forecasting of landfast ice in Foggy Island Bay, Alaska in support of ice road operations, Cold Reg. Sci. Technol., 201, https://doi.org/10.1016/j.coldregions.2022.103618, 2022.

Cooley, S. W. and Ryan, J. C.: Community-scale changes to landfast ice along the coast of Alaska over 2000–2022, Environ. Res. Lett., 19, https://doi.org/10.1088/1748-9326/ad1c7b, 2024.

Dammann, D. O., Eicken, H., Meyer, F. J., and Mahoney, A. R.: Assessing small-scale deformation and stability of landfast sea ice on seasonal timescales through L-band SAR interferometry and inverse modeling, Remote Sens. Environ., 187, 492–504, https://doi.org/10.1016/j.rse.2016.10.032, 2016.

Dammann, D. O., Eicken, H., Mahoney, A. R., Meyer, F. J., Freymueller, J. T., and Kaufman, A. M.: Evaluating landfast sea ice stress and fracture in support of operations on sea ice using SAR interferometry, Cold Reg. Sci. Technol., 149, 51–64, https://doi.org/10.1016/j.coldregions.2018.02.001, 2018a.

Dammann, D. O., Eriksson, L. E. B., Mahoney, A. R., Stevens, C. W., van der Sanden, J., Eicken, H., Meyer, F. J., and Tweedie, C. E.: Mapping Arctic Bottomfast Sea Ice Using SAR Interferometry, Remote Sens.-Basel, 10, https://doi.org/10.3390/rs10050720, 2018b.

Dammann, D. O., Eriksson, L. E. B., Mahoney, A. R., Eicken, H., and Meyer, F. J.: Mapping pan-Arctic landfast sea ice stability using Sentinel-1 interferometry, The Cryosphere, 13, 557–577, https://doi.org/10.5194/tc-13-557-2019, 2019.

Dammert, P. B., Lepparanta, M., and Askne, J.: SAR interferometry over baltic sea ice, Int. J. Remote Sens., 19, 3019–3037, https://doi.org/10.1080/014311698214163, 1998.

Danielson, S. L., Dobbins, E. L., Jakobsson, M., Johnson, M. A., Weingartner, T. J., Williams, W. J., and Zarayskaya, Y.: Sounding the Northern Seas, EOS, 96, https://eos.org/science-updates/sounding-northern-seas (last access: 14 June 2026), 2015.

Einhorn, A. H.: aheinhorn/Alaska_InSAR_CODE: Landfast ice stability from InSAR (INSAR_Paper_2026), Zenodo [code], https://doi.org/10.5281/zenodo.20692754, 2026.

Fedders, E., Mahoney, A., Dammann, D. O., Polashenski, C., and Hutchings, J.: Two-dimensional thermal and dynamical strain in landfast sea ice from InSAR: results from a new analytical inverse method and field observations, Ann. Glaciol., 65, 1–14, https://doi.org/10.1017/aog.2024.29, 2024.

Ferretti, A., Monti-Gaurnieri, A., Prati, C., and Rocca, F.: lnSAR Principles: Guidelines for SAR lnterf erometry Processing and Interpretation, Vol. TM-19, ESA Publications, ISBN 92-9092-233-8, 2007.

Fraser, A., Massom, R. A., Michael, K. J., Galton-Fenzi, B. K., and Lieser, J. L.: East antarctic landfast sea ice distribution and variability, 2000-08, J. Climate, 25, 1137–1156, https://doi.org/10.1175/JCLI-D-10-05032.1, 2012.

Fraser, A. D., Massom, R. A., Ohshima, K. I., Willmes, S., Kappes, P. J., Cartwright, J., and Porter-Smith, R.: High-resolution mapping of circum-Antarctic landfast sea ice distribution, 2000–2018, Earth Syst. Sci. Data, 12, 2987–2999, https://doi.org/10.5194/essd-12-2987-2020, 2020.

Fraser, A. D., Massom, R. A., Handcock, M. S., Reid, P., Ohshima, K. I., Raphael, M. N., Cartwright, J., Klekociuk, A. R., Wang, Z., and Porter-Smith, R.: Eighteen-year record of circum-Antarctic landfast-sea-ice distribution allows detailed baseline characterisation and reveals trends and variability, The Cryosphere, 15, 5061–5077, https://doi.org/10.5194/tc-15-5061-2021, 2021.

Friedl, P., Weiser, F., Fluhrer, A., and Braun, M. H.: Remote sensing of glacier and ice sheet grounding lines: a review, Earth-Sci. Rev., 2, https://doi.org/10.1016/j.earscirev.2019.102948, 2019.

George, J. C., Zeh, J., Suydam, R., and Clark, C.: Abundance and population trend (1978–2001) of western arctic bowhead whales surveyed near Barrow, Alaska, Mar. Mammal Sci., https://doi.org/10.1111/j.1748-7692.2004.tb01191.x, 2004.

Hogenson, K., Arko, S., Buechler, B., Hogenson, R., Herrmann, J., and Geiger, A.: Hybrid Pluggable Processing Pipeline (HyP3): A cloud-based infrastructure for generic processing of SAR data, in: AGU Fall Meeting, https://doi.org/10.5281/zenodo.4646138, 2016.

Hošeková, L., Eidam, E., Panteleev, G., Rainville, L., Rogers, W. E., and Thomson, J.: Landfast ice and coastal wave exposure in Northern Alaska, Geophys. Res. Lett., 48, https://doi.org/10.1029/2021GL095103, 2021.

Itkin, P., Losch, M., and Gerdes, R.: Landfast ice affects the stability of the Arctic halocline: evidence from a numerical model, J. Geophys. Res.-Oceans, 120, 2622–2635, https://doi.org/10.1002/2014JC010353, 2015.

Laidre, K. L., Stirling, I., Lowry, L. F., Wiig, Ø., Heide-Jørgensen, M. P., and Ferguson, S. H.: Quantifying the sensitivity of Arctic marine mammals to climate-induced habitat change, Ecol. Appl., https://doi.org/10.1890/06-0546.1, 2008.

Laidre, K. L., Stern, H., Kovacs, K. M., Lowry, L., Moore, S. E., Regehr, E. V., Ferguson, S. H., Wiig, Ø., Boveng, P., Angliss, R. P., Born, E. W., Litovka, D., Quakenbush, L., Lydersen, C., Vongraven, D., and Ugarte, F.: Arctic marine mammal population status, sea ice habitat loss, and conservation recommendations for the 21st century, Conserv. Biol., 29, 724–737, https://doi.org/10.1111/cobi.12474, 2015.

Lange, K. A., Lange, K. A., Bradley, A. C., Duncan, K., and Farrell, S. L.: Grounded ridge detection and characterization along the Alaska Arctic coastline using ICESat-2 surface height retrievals, The Cryosphere, 19, 2045–2065, https://doi.org/10.5194/tc-19-2045-2025, 2025.

Li, S., Shapiro, L., Mcnutt, L., and Jeffers, A.: Application of satellite radar interferometry to the detection of sea ice deformation, Journal of the Remote Sensing Society of Japan, 16, 153–163, 1996.

Libert, L., Wuite, J., and Nagler, T.: Automatic delineation of cracks with Sentinel-1 interferometry for monitoring ice shelf damage and calving, The Cryosphere, 16, 1523–1542, https://doi.org/10.5194/tc-16-1523-2022, 2022.

Lovvorn, J. R., Anderson, E. M., Rocha, A. R., Larned, W. W., Grebmeier, J. M., Cooper, L. W., Kolts, J. M., and North, C. A.: Variable wind, pack ice, and prey dispersion affect the long-term adequacy of protected areas for an Arctic sea duck, Ecol. Appl., 24, 396–412, https://doi.org/10.1890/13-0411.1, 2014.

Mahoney, A.: armahoney-seaice/SLIEalyzer: SLIEalyzer (v1.0), Zenodo [code], https://doi.org/10.5281/zenodo.17353613, 2025.

Mahoney, A. R. and Einhorn, A. H.: The evolving decline of landfast sea ice in Northern Alaska and adjacent waters: results from an updated climatology, J. Geophys. Res.-Oceans, 131, https://doi.org/10.1029/2025JC022464, 2026.

Mahoney, A., Eicken, H., Graves, A., and Shapiro, L.: Defining and locating the seaward landfast ice edge in Northern Alaska, Int. Conf. on Port and Ocean Eng. Under Arctic Conditions, 3, 991–1000, 2006.

Mahoney, A., Eicken, H., Gaylord, A. G., and Shapiro, L.: Alaska landfast sea ice: links with bathymetry and atmospheric circulation, J. Geophys. Res.-Oceans, 112, https://doi.org/10.1029/2006JC003559, 2007.

Mahoney, A. R., Eicken, H., Gaylord, A. G., and Gens, R.: Landfast sea ice extent in the Chukchi and Beaufort Seas: the annual cycle and decadal variability, Cold Reg. Sci. Technol., 103, 41–56, https://doi.org/10.1016/j.coldregions.2014.03.003, 2014.

Mahoney, A. R., Turner, K. E., Hauser, D. D. W., Laxague, N. J. M., Lindsay, J. M., Whiting, A. V., Witte, C. R., Goodwin, J., Harris, C., Schaeffer, R. J., Schaeffer, R., Betcher, S., Subramaniam, A., and Zappa, C. J.: Thin ice, deep snow and surface flooding in Kotzebue Sound: landfast ice mass balance during two anomalously warm winters and implications for marine mammals and subsistence hunting, J. Glaciol., 67, 1013–1027, https://doi.org/10.1017/jog.2021.49, 2021.

Mahoney, A., Bieniek, P., Danielson, S., Einhorn, A., Hedstrom, K., Jones, J., and Klenz, T.: Landfast Ice Climatology within the Arctic OCS, https://espis.boem.gov/FinalReports/BOEM_2024-034.pdf (last access: 15 June 2026), 2024.

Masterson, D. M.: State of the art of ice bearing capacity and ice construction, Cold Reg. Sci. Technol., 58, 99–112, https://doi.org/10.1016/j.coldregions.2009.04.002, 2009.

Meyer, F. J., Mahoney, A. R., Eicken, H., Denny, C. L., Druckenmiller, H. C., and Hendricks, S.: Mapping arctic landfast ice extent using L-band synthetic aperture radar interferometry, Remote Sens. Environ., 115, 3029–3043, https://doi.org/10.1016/j.rse.2011.06.006, 2011.

Moreira, A., Prats-Iraola, P., Younis, M., Krieger, G., Hajnsek, I., and Papathanassiou, K. P.: A tutorial on synthetic aperture radar, IEEE Geoscience and Remote Sensing Magazine, 1, 6–43, https://doi.org/10.1109/MGRS.2013.2248301, 2013.

Morris, K., Li, S., and Jeffries, M.: Meso- and microscale sea-ice motion in the East Siberian Sea as determined from ERS-1 SAR Data, J. Glaciol., 45, 370–383, https://doi.org/10.3189/s0022143000001878, 1999.

Otsu, N.: A threshold selection method from gray-level histograms, IEEE T. Syst. Man Cyb., 9, 62–66, https://doi.org/10.1109/TSMC.1979.4310076, 1979.

Pratt, J. W.: Mapping bottomfast sea ice in arctic lagoons using Sentinel-1 interferometery, https://ualaska.researchcommons.org/uaf_grad_geosci/290 (last access: 15 June 2026), 2022.

Wang, Z., Liu, J., Wang, J., Wang, L., Luo, M., Wang, Z., Ni, P., and Li, H.: Resolving and analyzing landfast ice deformation by insar technology combined with sentinel-1a ascending and descending orbits data, Sensors-Basel, 20, 1–16, https://doi.org/10.3390/s20226561, 2020.

Winebrenner, D. P., Holt, B., and Nelson, E. D.: Observation of autumn freeze-up in the Beaufort and Chukchi Seas using the ERS 1 synthetic aperture radar, J. Geophys. Res.-Oceans, 101, 16401–16419, https://doi.org/10.1029/96JC01292, 1996.

World Meteorological Organization: World Meterological Organization: WMO sea-ice nomenclature, Tech. rep., Geneva, https://library.wmo.int/idurl/4/41953 (last access: 15 June 2026), 2014.